Cu_2ZnSnS_4 as a potential photovoltaic material: A hybrid Hartree-Fock density functional theory study

Joachim Paier,[1] Ryoji Asahi,[2] Akihiro Nagoya,[2] and Georg Kresse[1]
[1]*Faculty of Physics, Universität Wien and Center for Computational Materials Science, Sensengasse 8/12, A-1090, Wien, Austria*
[2]*Toyota Central R&D Laboratories, Inc., Nagakute, Aichi 480-1192, Japan*
(Received 4 December 2008; revised manuscript received 23 February 2009; published 25 March 2009)

First-principles calculations for the potential photovoltaic material Cu_2ZnSnS_4 (CZTS) are presented using density functional theory and the Perdew-Burke-Ernzerhof exchange-correlation functional as well as using the Heyd-Scuseria-Ernzerhof (HSE) hybrid functional. The HSE results compare very favorably to experimental data for the lattice constants and the band gap, as demonstrated for CZTS and selected ternary chalcopyrites such as $CuInS_2$, $CuInSe_2$, $CuGaS_2$, and $CuGaSe_2$. Furthermore the HSE band structure is validated using G_0W_0 quasiparticle calculations. The valence band is found to be made up by an antibonding linear combination of Cu-3*d* states and S-3*p* states, whereas an isolated band made up by Sn-5*s* and S-3*p* states dominates the conduction band. In the visible wavelength, the optical properties are determined by transitions from the Cu-3*d*/S-3*p* states into this conduction band. Comparison of the optical spectra calculated in the independent-particle approximation and using time-dependent hybrid functional theory indicates very small excitonic effects. For the structural properties, the kesterite-type structure of $I\bar{4}$ symmetry is predicted to be the most stable one, possibly along with cation disorder within the Cu-Zn layer. The energy differences between structural modifications are well approximated by a simple ionic model.

DOI: 10.1103/PhysRevB.79.115126 PACS number(s): 71.20.Mq, 71.15.Mb, 78.20.−e

I. INTRODUCTION

To meet the ever increasing demand for energy and to cope with the limited fossil resources available, photovoltaic solar-energy production will become increasingly important. While the solar cells based on single-crystal silicon or III-V semiconductors exhibit already very high efficiency, much cheaper solar cells are required for general and wide spread application. The ternary chalcopyrites, such as $Cu(In,Ga)Se_2$, have attracted much attention in this respect, and the efficiency of these materials has already improved up to 20%.[1] These materials, however, contain heavy elements, in the former case In, and environmental regulations require the long-term reduction of such elements in deposited waste. The quaternary semiconductor Cu_2ZnSnS_4 (CZTS) is a relatively new photovoltaic material and expected to be interesting for environmentally amenable solar cells, as its constituents are nontoxic and abundant in the earth's crust.[2–11] CZTS thin films show *p*-type conductivity, a direct band gap of 1.44–1.51 eV, and high optical absorption ($\sim 1\times 10^4$ cm^{-1}).[5,9,10,12] However, the highest conversion efficiency of CZTS reported so far is 6.7%,[11] demanding further improvement.

Although the structure and transport properties of CZTS have been extensively studied experimentally,[2–11] to the best of our knowledge, there have been only a few first-principles investigations; Raulot *et al.*[13] reported chemical trends and defect chemistry among (II-IV)-coupled substitutions for In/Ga in $Cu(In,Ga)(S,Se)_2$ within the local-density approximation (LDA). Hence, an atomistic detailed understanding of the binding mechanism and electronic properties of CZTS is still missing, and to fill this gap is the main objective of the present work. Since density functional theory using the local-density approximation or the generalized gradient approximation often severely underestimates the band gap and overestimates the lattice constants, we have applied a hybrid functional in the present work. Hybrid functionals mix about 25% nonlocal Hartree-Fock exchange with 75% semilocal exchange. This usually opens the band gap, and for most semiconductors, excellent agreement between theory and experiment is found for the band gap.[14] As we will show in this work, this also applies to CZTS, and we furthermore confirm the calculated density of states using highly accurate quasiparticle methods (G_0W_0). An accurate description of the quasiparticle band structure is a prerequisite for a reliable prediction of the optical properties, which are ultimately one key factor determining the efficiency of solar cells. Therefore, we also present results for the optical properties of CZTS.

The work is structured in the following way. After discussing the computational methods employed in this study in Sec. II, details about the electronic, structural and optical properties of CZTS are presented in Sec. III. We summarize and conclude in Sec. IV.

II. COMPUTATIONAL DETAILS

Calculations were performed using the plane-wave projector augmented-wave (PAW) (Refs. 21 and 22) method applying the semilocal Perdew-Burke-Ernzerhof (PBE) (Ref. 23) exchange-correlation functional and the Heyd-Scuseria-Ernzerhof (HSE) (Ref. 24) hybrid functional as implemented in the Vienna *ab initio* simulation package (VASP) (Refs. 25 and 26) code. The HSE screening parameter was set to a value of 0.2 $Å^{-1}$.[27] Details on the implementation and results of the extensive tests of HSE in the framework of the PAW method can be found in the literature (Refs. 28–30). The PAW data sets with radial cutoffs of 1.2, 1.2, 1.3, and 1.0 Å for Zn, Cu, Sn, and S, respectively, were employed

TABLE I. Lattice parameters a_0 and c_0 (in Å) and band gaps E_g (eV) of some chalcopyrites as obtained using density functional theory (PBE) and hybrid functionals (HSE) compared to experimental values.

	$CuInSe_2$			$CuInS_2$			$CuGaSe_2$			$CuGaS_2$		
	PBE	HSE	Expt.	PBE	HSE	Expt.	PBE	HSE	Expt.	PBE	HSE	Expt.
a_0 (Å)	5.871	5.834	5.782[a]	5.568	5.537	5.523[b]	5.685	5.637	5.596[c]	5.377	5.357	5.347[b]
c_0 (Å)	11.79	11.72	11.62[a]	11.25	11.20	11.13[b]	11.22	11.12	11.00[c]	10.61	10.53	10.47[b]
E_g (eV)	−0.35	0.85	1.04[d]	−0.01	1.33	1.53[e]	0.03	1.40	1.68[f]	0.70	2.22	2.43[e]

[a]Reference 15.
[b]Reference 16.
[c]Reference 17.
[d]Reference 18.
[e]Reference 19.
[f]Reference 20.

using a plane-wave cutoff energy of 350 eV. We also applied the G_0W_0 method[31] using the HSE eigenvalues and wave functions as initial input for the quasiparticle calculations.[32–34] The optical properties were determined in the independent-particle approximation using PBE and HSE, as well as, using the time-dependent HSE (TD-HSE) method.[35] The last method accounts for the electrostatic interaction between electrons and holes, and should give very accurate results for the absorption spectrum as well as for the static dielectric properties.

Brillouin-zone integration was performed on Γ-centered symmetry reduced Monkhorst-Pack[36] meshes using a Gaussian-smearing approach with $\sigma=0.01$ eV, except for the calculation of total energies and densities of states (DOSs), as well as PBE/HSE independent-particle spectra. For those calculations, the tetrahedron method with Blöchl corrections[37] was used. The crystal structures were optimized using an $8\times8\times8$ k mesh for the base-centered-tetragonal (bct) unit cells (8 atoms/cell) or an $8\times8\times4$ k mesh for the twice as large tetragonal unit cells (16 atoms/cell). HSE structure optimizations have been carried out using a more approximate $6\times6\times6$ and a $6\times6\times4$ k mesh for the bct and tetragonal unit cells, respectively.

In order to check the pertinence of applying the bct unit cells for kesterite (space group $I\bar{4}$) and stannite (space group $I\bar{4}2m$), we repeated the structure optimizations and energy calculations using the larger tetragonal unit cells. PBE structural parameters a_0 and c_0 for the bct and the tetragonal unit cells differed by at most 0.04 Å, whereas the HSE lattice constants differed by 0.016 Å (0.1%). PBE total energies where reproduced by the bct unit cell within 1 meV, while the HSE energies were uniformly shifted by about 150 meV, regarded as sufficiently accurate considering the appreciable computational work-load.

PBE and HSE DOS have been calculated using an $8\times8\times8$ or $8\times8\times4$ k mesh, whereas the G_0W_0 DOS was obtained using $6\times6\times6$ k points. For the optical calculations of the PBE independent-particle spectra, the tetrahedron method with $16\times16\times16$ k points and 476 conduction bands was used, whereas in the HSE case a total of 44 conduction bands was applied. For the TD-HSE absorption spectra (Sec. III C), Gaussian smearing ($\sigma=0.01$ eV) and a $24\times24\times24$ k mesh, mimicked by symmetry adapted shifts of a Γ-centered $6\times6\times6$ k mesh, was applied (see Ref. 35). The number of conduction bands involved in the TD-HSE calculations was set to 28.

To illustrate the accuracy of the HSE functional, we have calculated lattice constants and band gaps for the ternary chalcopyrites $Cu(In,Ga)(S,Se)_2$, which are closely related to CZTS. The results are shown in Table I. They clearly demonstrate that the HSE functional systematically improves upon the PBE lattice constants. Agreement with experiment is typically 1% for all of the considered compounds, although a trend toward too large lattice constants is observed for the compounds containing chalcogenides from the fifth row (Te). More importantly, the HSE functional predicts the band gaps reasonably well, while the PBE functional results in a significant underestimation of the band gap, with incorrect band ordering (negative band gaps) for CuIn compounds.

III. RESULTS AND DISCUSSION

A. Structural properties

Cu_2ZnSnS_4 crystallizes in the kesterite structure, which is shown in Fig. 1(a). The most important structural modification is stannite [Fig. 1(b)], which is observed for the closely related Cu_2FeSnS_4 (CFTS). For details we refer the reader to Ref. 2. Similar to ZnS or ZnO, all cations and anions are located in a tetrahedral bonding environment, with a stacking that is similar to zincblende. The different structural modifications are related to a different order in the cation sublattice. Kesterite is characterized by alternating cation layers of CuSn, CuZn, CuSn, and CuZn at $z=0$, 1/2, 1/2, and 3/4, respectively. The primitive cell is bct, whereas in Fig. 1(a) the tetragonal supercell is shown. In stannite, ZnSn layers alternate with Cu_2 layers, the primitive cell being again bct.[2] In addition to kesterite and stannite, we included three structural modifications of kesterite in our study, which are shown in Figs. 1(c)–1(e). These modifications belong to the tetragonal space groups $P\bar{4}2c$, $P\bar{4}2_1m$, and $P2$, respectively. All three can be considered to be modifications of kesterite, where the modifications are restricted to the exchange of two ions on the cation sublattice. In the structure shown in Fig. 1(c), Cu and Zn atoms in the layer $z=1/4$ are exchanged, creating a "stacking" fault with respect to the bct kesterite structure. In the structure shown in Fig. 1(d), Cu and Zn atoms are exchanged between two layers to yield complete Zn and Cu layers at $z=1/4$ and $z=3/4$. In the final structure Fig. 1(e), a Cu atom at $z=1/2$ is exchanged with the Zn atom at $z=3/4$. This recovers the stannite structure at the layers

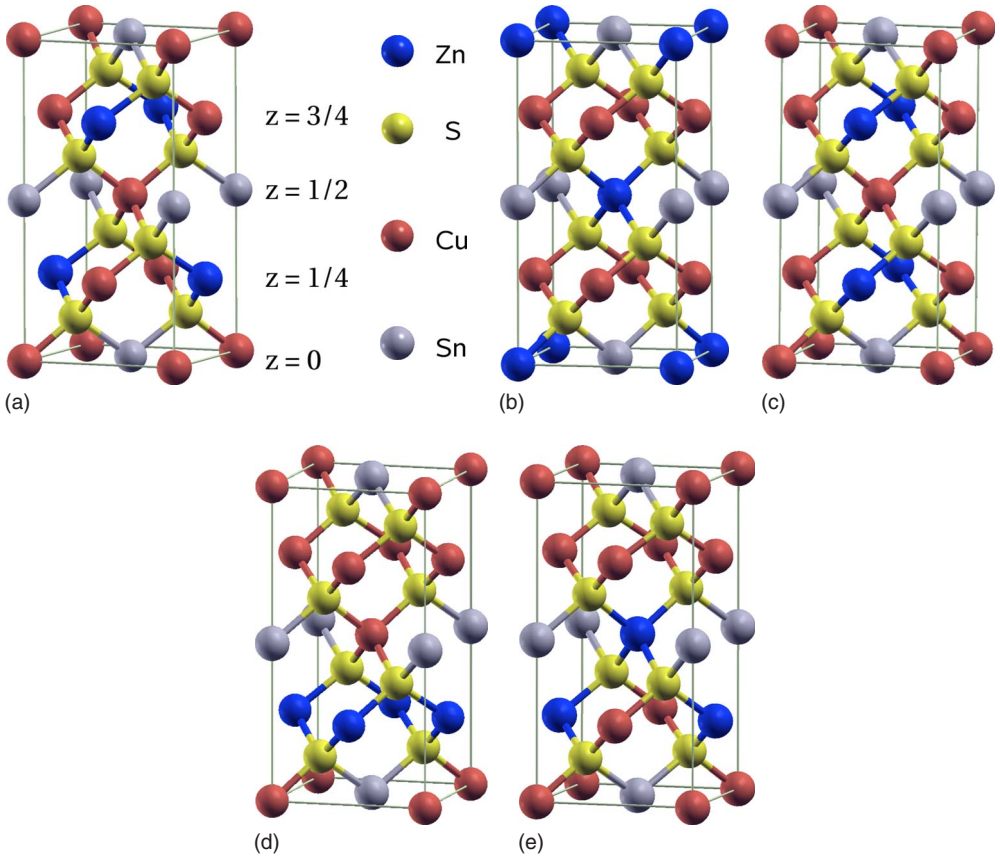

FIG. 1. (Color online) Schematic representations of the (a) kesterite and (b) stannite structures, emphasizing the difference in metal ordering. In addition, schematic representations of three structural modifications of kesterite are shown (c, d, and e), which are members of the $P\bar{4}2c$, $P\bar{4}2_1m$, and $P2$ space group, respectively. Atomic sphere radii are chosen arbitrarily.

$z=1/2$ and $z=3/4$, but maintains the kesterite structure in the other two layers. Although this selection is nonexhaustive, it covers some important modifications: cation disorder in the CuZn layer and cation disorder between Cu and Zn layers, which are both difficult to measure experimentally since Cu and Zn posses very similar atomic masses. Furthermore, structural mixtures between kesterite and stannite are covered.

Table II summarizes the predicted lattice parameters for the five modifications shown in Fig. 1. In agreement with experiment, kesterite is the most stable modification both for PBE as well as for HSE, but the $P\bar{4}2c$ modification is very close in energy. This is in agreement with experimental observations, where a considerable intermixing of the Cu and Zn atoms is observed within the Cu-Zn plane [compare (a) with (c) in Fig. 1]. The stannite structure is slightly higher in

TABLE II. Lattice parameters a_0, b_0, and c_0 (in Å) of modifications of CZTS as obtained using density functional theory (PBE) and hybrid functionals (HSE) compared to experimental values. Energy differences ΔE (eV) to the kesterite structure and the band gaps E_g (eV) are also listed.

Type		Kesterite		Stannite		Modification					
Symmetry		$I\bar{4}$		$I\bar{4}2m$		$P\bar{4}2c$		$P\bar{4}2_1m$		$P2$	
	Expt.	PBE	HSE	PBE	HSE	PBE	HSE	PBE	HSE	PBE	HSE
a_0 (Å)	5.427[a]	5.466	5.448	5.460	5.438	5.466	5.446	5.478	5.464	5.473	5.443
b_0 (Å)										5.478	5.452
c_0 (Å)	10.871[a]	10.929	10.889	10.976	10.941	10.929	10.885	10.942	10.857	10.939	10.892
$c_0/2a_0$	1.001	1.000	0.999	1.005	1.006	1.000	0.999	0.999	0.993	0.999	1.001
ΔE (eV)		0.0	0.0	0.046	0.054	0.005	0.012	0.271	0.390	0.195	0.272
E_g (eV)	1.44–1.51[b]	0.096	1.487	−0.030	1.295	0.071	1.458	−0.097	1.206	−0.111	1.073

[a]Reference 2.
[b]References 5, 9, and 10.

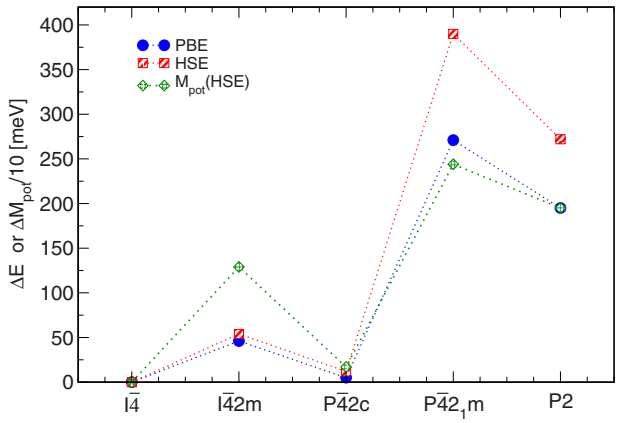

FIG. 2. (Color online) Total energy differences obtained using PBE (blue circles) and HSE (red hatched squares), as well as the effective Madelung energy differences, where the energy zero refers to (the most stable) kesterite structure (space group $I\bar{4}$). The electrostatic Madelung energy has been divided by 10 (see text).

energy (50 meV), whereas the other two modifications $P\bar{4}2_1m$ and $P2$ are much higher in energy (200–400 meV).

To understand the origin for this particular energy order, we resort to a simple Madelung model, in which we assign "effective ionic charges" to each individual atom, i.e., Cu^{+}, Zn^{2+}, Sn^{3+}, and $S^{1.75-}$. The charges for Sn and S ions are justified by taking covalent bonding between Sn and S into consideration (see Sec. III B). To account for the strong electronic screening in CZTS, we have divided the Madelung energies by a factor 10, which is close to the predicted dielectric constant (see Sec. III C). The results are shown together with the calculated energy differences for PBE and HSE in Fig. 2. It is quite remarkable that despite its exceeding simplicity and the neglect of Pauli repulsion, the model roughly predicts the *ab initio* energy differences. For instance, the near degeneracy of the kesterite and $P\bar{4}2c$ modification is readily observed, as well as the stability of kesterite compared to all other structural modifications. This confirms that the usually applied ionic picture for CZTS essentially captures the bonding situation correctly; in other words, covalency plays only a minor role for the energetics of CZTS.

Table II also summarizes the band gaps for all five modifications. As already mentioned, PBE underestimates the band gaps severely, and resultantly all modifications but kesterite and $P\bar{4}2c$ are predicted to be metals using PBE. The hybrid HSE functional gives certainly a better account for the band gap, and sizeable band gaps are predicted for all five modifications with the largest band gaps for kesterite and the $P\bar{4}2c$ modification. The most important result is that kesterite and $P\bar{4}2c$ possess virtually identical band gaps, indicating that cation disorder within the Cu-Zn layer will hardly modify the optical properties, but it may reduce mobility of carriers due to the potential disorder.

B. Electronic properties

Sn is generally considered to prefer an oxidation state of +4 in ionic compounds, and it is common practice to regard

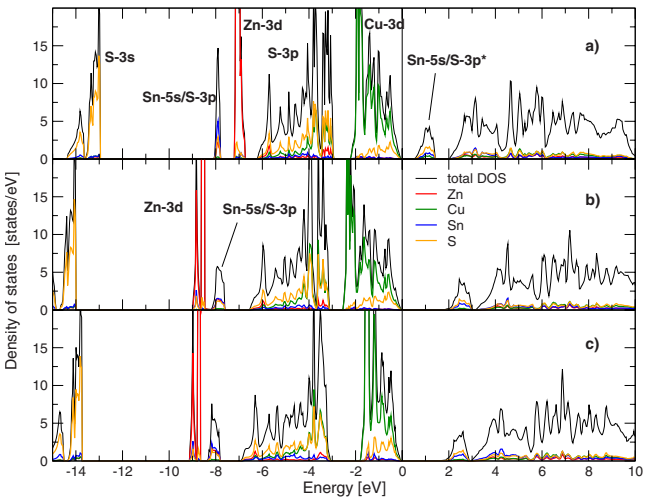

FIG. 3. (Color online) Total and orbital-projected density of states of CZTS kesterite calculated using (a) PBE, (b) HSE, and (c) G_0W_0(HSE) (see text). The origin of energy (vertical line) is set to the valence-band maxima.

CZTS as an ionic material associating the following formal valencies with the atoms: Cu^{+}, Zn^{2+}, Sn^{4+}, and S^{2-}. For instance, ^{57}Fe and ^{119}Sn Mössbauer spectroscopic and magnetic-susceptibility data collected on CFTS stannite by Eibschütz *et al.*[38] suggest $Cu_2^{+}Fe^{2+}Sn^{4+}S_4^{2-}$. Due to the similarity of CFTS stannite with CZTS kesterite[6] the same arguments may apply to the cationic valencies in CZTS kesterite.

In order to analyze the chemical bonding, we will concentrate on the electronic properties of kesterite CZTS. The total density of states, as well as the atom projected density of states are shown in Fig. 3 using various approximations for the exchange-correlation functional (PBE, HSE) as well as G_0W_0. It is observed that different approximations to the functional change the absolute position of the peaks, but the qualitative features are independent of the exchange-correlation functional. Therefore, we will concentrate on the conventional density functional theory results, i.e., PBE first.

The S-3*s* and S-3*p* states are clearly visible at −14 to −13 eV and −6 to −3 eV, respectively. The Zn-3*d* states form a very narrow band located −7 eV below the Fermi level, and the valence band is clearly made up of Cu-3*d* states (−2 to 0 eV). Furthermore, a sizeable hybridization between S-3*p* and Cu-3*d* is recognized in the energy range between −6 and 0 eV. In fact, the Cu-3*d* states are split into lower e_g and higher t_{2g} orbitals in the tetrahedral crystal field. The former are nonbonding and appear as a sharp weakly hybridized peak around −2 eV. On the other hand, the latter strongly hybridize with S-3*p* orbitals to create bonding (−6 to −3 eV) and antibonding (−1.5 to 0 eV) states. Since the bonding S-3*p*/Cu-3*d* and antibonding Cu-3*d*/S-3p^{*} linear combinations are fully occupied, the net interaction is Pauli repulsion rather than crystal stability. The charge density corresponding to the top of the valence band is shown in Fig. 4. The top of the valence band is almost triple degenerated, as expected from the t_{2g} character. The charge density is mostly located at the Cu atoms (70%). However, a sizable contribution of antibonding S-3*s* states (30%) with some small admixture of S-3*p* states is also recognized.

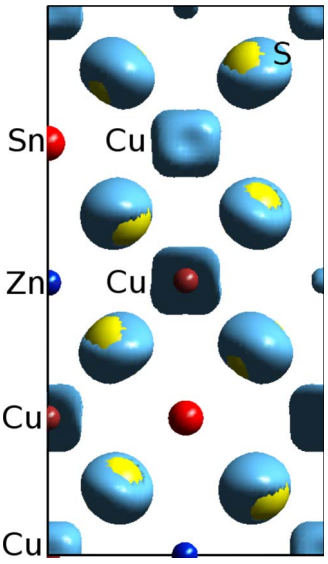

FIG. 4. (Color online) Charge density calculated for the three bands at the top of the valence band at Γ. Color coding of atoms is similar to Fig. 1. View is along the [100] direction. Similar to Fig. 1, two unit cells are shown, starting with the CuZn layer at the bottom.

In PBE, the first conduction band is separated by a gap of 0.1 eV from the valence band and contains a single state. This low lying conduction band is separated from the rest of the conduction bands by a gap of 0.5 eV. On the basis of the previous arguments regarding the valency, one would expect that the first conduction band is made up of Sn-5*s* states, and a sizeable contribution of Sn-5*s* states (blue) is indeed recognized in the DOS. However, the density of states suggests that the yet presented picture is an oversimplification: the Sn-5*s* states dominate a very narrow band located 8 eV below the conduction band. The band is made up of a bonding linear combination of the Sn-5*s* and S-3*p* orbitals (Sn-5*s*/S-3*p*). Vice versa, the first conduction band is made up of the corresponding antibonding linear combination of Sn-5*s* and S-3*p* (Sn-5*s*/S-3p^*) states. To substantiate this covalent picture, the electronic charge density arising from the band located at −7 eV (Sn-5*s*/S-3*p*), and the charge density corresponding to the first conduction band (Sn-5*s*/S-3p^*) are shown in Fig. 5. The left panel confirms that in the Sn-5*s*/S-3*p* orbital, a sizeable contribution of S-3*p* states is admixed to the dominant spherical Sn-5*s* orbital. The Zn-3*d* orbitals are also involved. On the other hand, the first conduction band (Sn-5*s*/S-3p^*) exhibits a nodal plane (zero charge) between the Sn and the S atoms. The resulting charge depletion along the bond causes an indentation of the isosurface. One also recognizes that the Cu-3*d* states contribute slightly to the conduction band.

Covalent bonding also modifies the Born-effective charges (dynamical charges) that describe how much charge moves when an atom is displaced from its ground-state position. In completely ionic compounds, one would expect charges identical to the formal valencies of each atom: Cu^{1+}, Zn^{2+}, Sn^{4+}, and S^{2-}. For the S atoms, however, we find fairly large off-diagonal components and nonisotropic diagonal components (HSE functional: −1.85, −1.55, −1.76, average

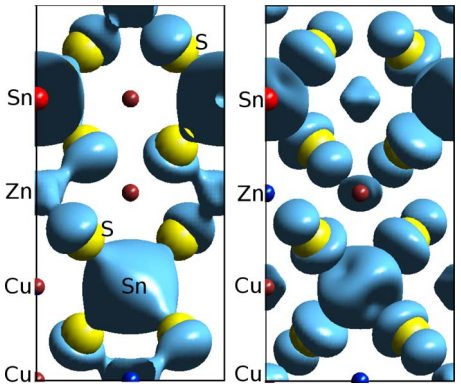

FIG. 5. (Color online) Charge density corresponding to the Sn-5*s*/S-3*p* state (left) and first conduction band Sn-5*s*/S-3p^* (right). See Fig. 4 for details.

−1.72), confirming the previously discussed non-negligible covalent contribution to the bond. On the other hand, for the cations almost isotropic values of 0.84, 2.1, and 3.2 are found for Cu, Zn, and Sn, respectively (HSE functional). The fully ionic character of Cu and Zn is thereby confirmed, and the Sn ionicity of roughly 3 is in accordance with the previous picture: the occupied Sn-5*s*/S-3*p* band holds a total of two electrons, and due to the hybrid character of this band one electron is effectively transferred to the Sn atom, yielding a covalency closer to +3 than the expected +4.

Our results are summarized in a molecular interaction diagram shown in Fig. 6. The one-electron energies calculated for atoms are shown in three light shaded boxes divided into Zn/Sn, S, and Cu. The resulting bonding and antibonding states are shown in between, and the final DOS is schematically sketched to the right. A similar bonding structure appears in ternary I-III-VI_2 chalcopyrite semiconductors, such as $CuInSe_2$ and $CuGaSe_2$, where III-*s*/VI-*p* bonding states constitute the conduction-band minimum (CBM) as previously reported.[39] In the case of CZTS, the CBM consists mainly of Sn-5*s*/S-3p^* states and there is no contribution from Zn-4*s* as the result of the much higher atomic energy of Zn-4*s* than that of Sn-5*s*. The only not mentioned point yet is that Sn-5*p*, Zn-4*s*, and Cu-4*s* orbitals are formally unoccupied in CZTS (ionic picture). However, the DOS suggests that these orbitals are hybridized with S-3*p* contributing to the states in the valence band in the energy range between −6 and −4 eV (marked A in Fig. 6). The second conduction band is found at energies greater than 2 eV (marked A^* in Fig. 6), and it is dominated by these atomic orbitals but also contains some admixture of S-3*p* states.

We turn now briefly to the electronic properties calculated using hybrid functionals. The HSE DOS differs qualitatively very little from the PBE DOS as shown in Fig. 3. Inclusion of nonlocal exchange increases the overall band width and opens the band gap from 0.1 to 1.5 eV. As for many materials,[27] the agreement with the experimental band gap is exceptionally good at the HSE level [expt.: 1.44–1.51 eV (Refs. 5, 9, and 10)]. The other relevant observation is that the Zn-3*d* band has moved toward larger binding energies and is now located below the Sn-5*s*/S-3*p* band, which is a result of the reduced self-interaction for localized orbitals

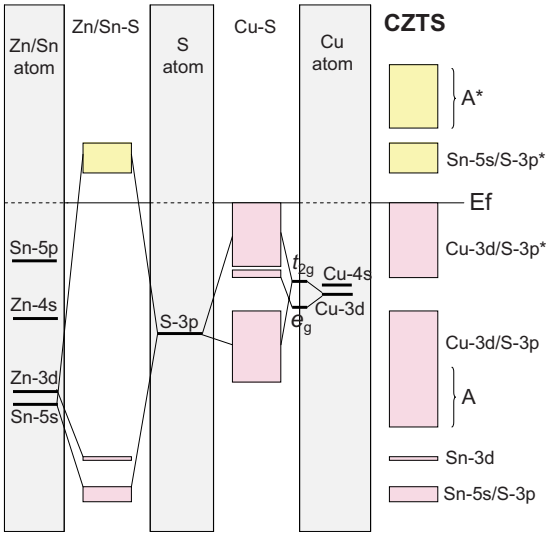

FIG. 6. (Color online) Molecular interaction diagram schematically illustrating the atomic one-electron energies (light gray) and the band structure of CZTS (rightmost), as well as emerging cation-S hybrid bands (e.g., Sn-5*s* with S-3*p*). Hybridization of Cu-4*s*, Zn-4*s*, and Sn-5*p* states results in the bonding linear combinations marked by A, and antibonding linear combinations A* that make up the second conduction band. Note that the atomic levels include neither any potential shifts due to ionization nor alignment of the vacuum level with respect to the Fermi energy.

using hybrid functionals. Similarly, the S-3*s* states are now located at larger binding energies. We expect that the HSE description is more accurate than the PBE one, since PBE notoriously underestimates the binding energies of localized electrons. The important point, however, is that HSE predicts again a conduction band with Sn-5*s*/S-3*p** character that is well separated from the valence and other conduction bands.

The final panel in Fig. 3 shows the G_0W_0 results. These results were obtained using the HSE wave functions and one-electron energies as a starting point. This is usually a better approximation than simple LDA-based G_0W_0.[34,35] In the present case, the serious underestimation of the band gap in the LDA yields unrealistic screening properties (see below) and resultantly much too small band gaps in LDA-based G_0W_0 calculations. The HSE-based G_0W_0 quasiparticle energies agree very well with the HSE one-electron energies. The only difference is a reduction in the band width of the Cu-3*d* band. It is well documented that gradient corrected functionals overestimate the band width of Cu 3*d* states, whereas G_0W_0 yields a reasonable description.[40] We therefore expect that the HSE G_0W_0 results are more reliable than HSE, and that the final panel approximates the true quasiparticles very well. Experimental confirmation of this spectrum would certainly be highly desirable. *A posteriori*, the agreement between the G_0W_0 quasiparticle spectrum and the HSE band structure also indicates that the correct physics is accounted for by the hybrid functional.

To analyze the electronic and transport properties in more detail, the band structure of CZTS is shown in Fig. 7 for PBE and HSE. As already emphasized, the valence bands are made up of ten Cu-3*d* bands (two Cu atoms/unit cell), eleven S-3*p* bands, five Zn-3*d* band and the already discussed

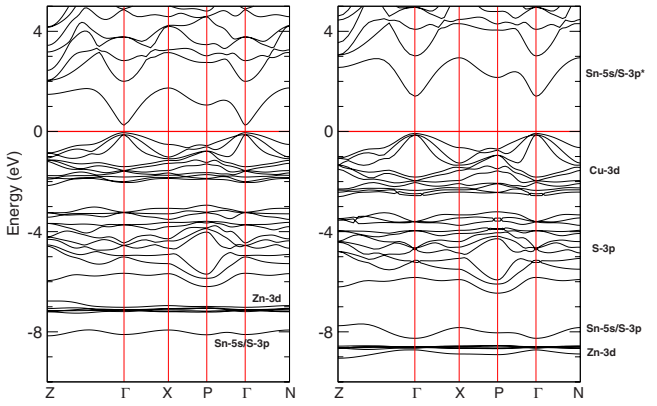

FIG. 7. (Color online) PBE (left panel) and HSE (right panel) band structures of CZTS kesterite.

Sn-5*s*/S-3*p* band (giving a total of 12 S-3*p* related bands). The band gap is direct and occurs at the Γ point. The conduction band is made up of the single Sn-5*s*/S-3*p** band, which has been discussed before. The dispersion of that band is 1.5 eV with maxima occurring at the X point. Again, it is clearly recognized that this single band is well separated from the rest of the conduction band. For both computational schemes (HSE and PBE), the band topology is very similar, as far as the conduction band is concerned, since HSE essentially shifts the conduction bands to higher energies (similar to a scissor correction).

C. Optical properties

The predicted dielectric functions are shown in Fig. 8 for PBE and HSE. We first concentrate on the imaginary part and the independent-particle spectra (PBE-IP and HSE-IP) shown as red and black thin lines, respectively. As one would expect, the PBE-IP and HSE-IP spectra differ only little. Essentially, the HSE spectrum is blue shifted and somewhat reduced in intensity. This reduction is required by the *f*-sum rule, which states that the imaginary part of the dielectric function, ε_2, observes

$$\int_0^\infty \varepsilon_2(\omega)\omega d\omega = \text{constant},$$

independent of the one-particle wave functions. For this relationship to hold, a blueshift from ω to $\omega+\Delta\omega$ must reduce the intensity by a factor $\frac{\omega}{\omega+\Delta\omega}$. The HSE spectrum can be almost quantitatively obtained by applying this particular scaling relation and a scissor correction of $\Delta\omega \approx 1.2$ eV. This semiempirical scaling relation also explains why the first shoulder in the HSE spectrum at 1.9 eV is much less pronounced than the first shoulder in the PBE spectrum at 0.7 eV.

The most accurate optical spectrum is obtained using TD-HSE (thick black line). Compared to the HSE-IP spectrum, TD-HSE includes an electrostatic interaction between the excited particles and created holes. The resultant TD-HSE equation is similar to the Bethe-Salpeter equation (BSE), but approximates the kernel for the electrostatic interaction between particles and holes by 1/4 of the screened exchange,

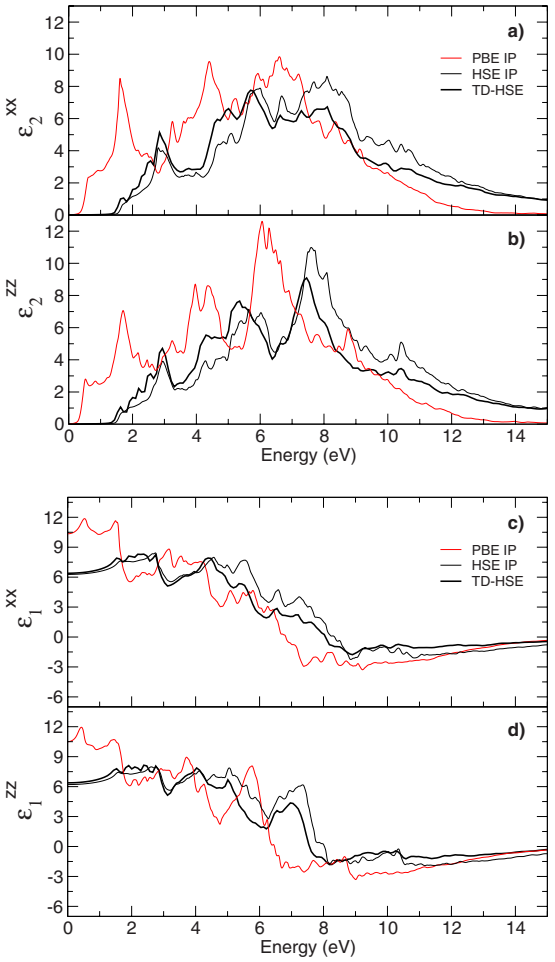

FIG. 8. (Color online) Imaginary and real parts of the dielectric function for CZTS kesterite. Panels (a) and (b) show the imaginary parts of the dielectric function using PBE, HSE in the independent-particle (IP) approximation, and TD-HSE for light polarized in a and c directions, respectively. Similarly, the real parts of the dielectric function are shown in panels (c) and (d).

whereas BSE determines the kernel from the dielectric screening properties itself. Since HSE works so well for the one-electron states (see Fig. 3), we expect it to be accurate for the two-particle spectrum as well. Additionally, Paier *et al.*[35] recently demonstrated that TD-HSE is a fairly good approximation for semiconductors.

As a result of the electrostatic particle-hole interaction, intensity is shifted from higher excitation energies to lower excitation energies, and high energy peaks become slightly redshifted. But for CZTS, the changes from the independent-particle approximation to the more accurate interacting approximation (particle-hole interaction) is only quantitative. In particular, a bound exciton, i.e., onset of optical absorption below the energy of the fundamental gap, is not predicted by our calculations.

The static dielectric constants could be estimated from the real part of the dielectric function ε_1 for $\omega \to 0$. In practice we used a finite field approach avoiding a summation over empty states.[35] We found values of 6.49 and 6.47 for TD-HSE parallel to a and c, respectively, which implies *de facto* isotropic screening. The PBE-IP approximation predicts a much larger value of 10.3, but because of the serious underestimation of the gap in PBE, this value is expected to be much too large. On the basis of the experience for other materials, such as Si, ZnO, or ZnS, we expect the present TD-HSE predictions to be accurate to within 5%.[35] To completely determine the dielectric properties, we have also calculated the ionic contributions to the static dielectric function. This was done in the simpler PBE approximation, but because the ionic contributions depend on the Born-effective charges and the vibrational modes only, which are usually accurately predicted using gradient-corrected density functionals, we expect this approximation to be very reliable. The actual calculations were performed using the method recently suggested by Wu *et al.*[41] We found contributions of 2.6 and 3.3 parallel to the a and c axis, respectively. Therefore, the total static dielectric constants are 9.1 and 9.8 parallel to a and c.

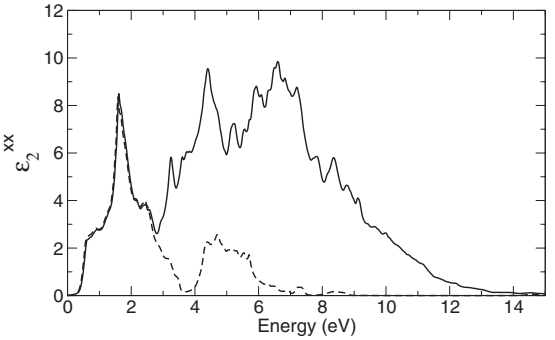

FIG. 9. Imaginary part of the PBE dielectric function for CZTS kesterite. The full line represents the spectrum obtained using 476 conduction bands, whereas the dashed line shows the spectrum involving transitions into the first conduction band only (see Fig. 7).

To determine which transitions are responsible for the energy range relevant to solar-light absorption, we have calculated the dielectric functions in the independent-particle approximation within PBE considering scattering into the first conduction band only, i.e., from Cu-3d/S-3p states into the Sn-5s/S-3p^* band. The results are compared to the full spectrum in Fig. 9. As expected, the resultant spectrum is identical to the full spectrum in PBE up to 2 eV, which covers the first strong peak located around 3 eV in the HSE spectrum. We furthermore note that transitions into the Sn-5s/S-3p^* band are also possible between 4 and 6 eV, being related to transitions from the S-3p states into the conduction band; nevertheless, in this part of the spectrum, other transitions dominate. Since the energy region absorbed by solar cells is typically less than 3 eV,[11] the most relevant transitions are the electron excitations from the Cu-3d/S-3p bands into the Sn-5s/S-3p^* band. Crucial for the fairly large absorption coefficient at this energy, is the sizeable admixture of S-3p states to both bands.

IV. CONCLUSIONS

In conclusion, first-principles investigations based on the PBE functional and HSE hybrid functional have been carried out for the potential photovoltaic material CZTS to clarify its

ground-state structure, electronic structure, and optical properties. Our results can be summarized as follows: (i) The ground-state calculations predict that the kesterite structure with the $I\bar{4}$ symmetry is the most stable one, but exchange of Cu and Zn atoms in the CuZn layer costs only very little energy. This is consistent with experiment where considerable intermixing of the Cu and Zn atoms within the Cu-Zn plane is observed. (ii) The structural stability is described by a simple ionic picture as demonstrated by equivalent energy ordering for the *ab initio* calculations and a simple Madelung model. Only one strong covalent feature is observed in the density of states; the Sn-5*s* and S-3*p* states hybridize resulting in an occupied bonding state about 8 eV below the top of the valence band, and an antibonding state making up the conduction band. As a consequence, the ionic charges of Sn and S are rather +3 and −1.75 than +4 and −2. (iii) The antibonding Sn-5*s*/S-3p^* orbital makes up the first conduction band. This conduction band is isolated from the remaining conduction bands by about 0.2 eV, and the predicted band gap between the conduction and valence band is 1.5 eV using the hybrid HSE functional. The top of valence band, on the other hand, is dominated by Cu t_{2g} orbitals hybridized with S-3*p* states. (iv) The optical-absorption coefficient, which is proportional to the imaginary part of the dielectric function, is fairly large in the energy range of visible light. Absorption in this energy range is completely dominated by transitions from the Cu t_{2g} orbitals into the Sn-5*s*/S-3p^* band. Crucial for the fairly large absorption coefficient, is certainly the admixture of antibonding S-3p^* orbitals to both states.

ACKNOWLEDGMENT

This work was partially supported by the Austrian Fonds zur Förderung der wissenschaftlichen Forschung within the START Grant No. Y218.

[1] I. Repins, M. A. Contreras, B. Egaas, C. DeHart, J. Scharf, C. L. Perkins, B. To, and R. Noufi, Prog. Photovoltaics **16**, 235 (2008).
[2] S. R. Hall, J. T. Szymanski, and J. M. Stewart, Can. Mineral. **16**, 131 (1978).
[3] G. P. Bernardini, D. Borrini, A. Caneschi, F. Di Benedetto, D. Gatteschi, S. Ristori, and M. Romanelli, Phys. Chem. Miner. **27**, 453 (2000).
[4] H. Katagiri, N. Ishigaki, T. Ishida, and K. Saito, Jpn. J. Appl. Phys. **40**, 500 (2001).
[5] J.-S. Seol, S.-Y. Lee, J.-C. Lee, H.-D. Nam, and K.-H. Kim, Sol. Energy Mater. Sol. Cells **75**, 155 (2003).
[6] F. Di Benedetto, G. P. Bernardini, D. Borrini, W. Lottermoser, G. Tippelt, and G. Amthauer, Phys. Chem. Miner. **31**, 683 (2005).
[7] S. Schorr, H.-J. Hoebler, and M. Tovar, Eur. J. Mineral. **19**, 65 (2007).
[8] N. Kamoun, H. Bouzouita, and B. Rezig, Thin Solid Films **515**, 5949 (2007).
[9] H. Matsushita, T. Maeda, A. Katsui, and T. Takizawa, J. Cryst. Growth **208**, 416 (2000).
[10] J. J. Scragg, P. J. Dale, and L. M. Peter, Electrochem. Commun. **10**, 639 (2008).
[11] H. Katagiri, K. Jimbo, S. Yamada, T. Kamimura, W. S. Maw, T. Fukano, T. Ito, and T. Motohiro, Appl. Phys. Express **1**, 041201 (2008).
[12] K. Ito and T. Nakazawa, Jpn. J. Appl. Phys. **27**, 2094 (1988).
[13] J. M. Raulot, C. Domain, and J. F. Guillemoles, J. Phys. Chem. Solids **66**, 2019 (2005).
[14] J. Heyd, J. E. Peralta, G. E. Scuseria, and R. L. Martin, J. Chem. Phys. **123**, 174101 (2005).
[15] J. Parkes, R. D. Tomlinson, and M. J. Hampshire, J. Appl. Crystallogr. **6**, 414 (1973).
[16] S. C. Abrahams and J. L. Bernstein, J. Chem. Phys. **59**, 5415 (1973).
[17] S. C. Abrahams and J. L. Bernstein, J. Chem. Phys. **61**, 1140 (1974).
[18] J. L. Shay, B. Tell, H. M. Kasper, and L. M. Schiavone, Phys. Rev. B **7**, 4485 (1973).
[19] B. Tell, J. L. Shay, and H. M. Kasper, Phys. Rev. B **4**, 2463 (1971).
[20] J. L. Shay, B. Tell, H. M. Kasper, and L. M. Schiavone, Phys. Rev. B **5**, 5003 (1972).
[21] P. E. Blöchl, Phys. Rev. B **50**, 17953 (1994).
[22] G. Kresse and D. Joubert, Phys. Rev. B **59**, 1758 (1999).
[23] J. P. Perdew, K. Burke, and M. Ernzerhof, Phys. Rev. Lett. **77**, 3865 (1996).
[24] J. Heyd, G. E. Scuseria, and M. Ernzerhof, J. Chem. Phys. **118**, 8207 (2003).
[25] G. Kresse and J. Furthmüller, Comput. Mater. Sci. **6**, 15 (1996).
[26] G. Kresse and J. Furthmüller, Phys. Rev. B **54**, 11169 (1996).
[27] A. V. Krukau, O. A. Vydrov, A. F. Izmaylov, and G. E. Scuseria, J. Chem. Phys. **125**, 224106 (2006).
[28] J. Paier, R. Hirschl, M. Martijn, and G. Kresse, J. Chem. Phys. **122**, 234102 (2005).
[29] J. Paier, M. Marsman, G. Kresse, I. C. Gerber, and J. Ángyán, J. Chem. Phys. **124**, 154709 (2006).
[30] J. Paier, M. Marsman, G. Kresse, I. C. Gerber, and J. Ángyán, J. Chem. Phys. **125**, 249901 (2006).
[31] L. Hedin, Phys. Rev. **139**, A796 (1965).
[32] M. Shishkin and G. Kresse, Phys. Rev. B **74**, 035101 (2006).
[33] M. Shishkin and G. Kresse, Phys. Rev. B **75**, 235102 (2007).
[34] F. Fuchs, J. Furthmuller, F. Bechstedt, M. Shishkin, and G. Kresse, Phys. Rev. B **76**, 115109 (2007).
[35] J. Paier, M. Marsman, and G. Kresse, Phys. Rev. B **78**, 121201(R) (2008).
[36] H. J. Monkhorst and J. D. Pack, Phys. Rev. B **13**, 5188 (1976).
[37] P. E. Blöchl, O. Jepsen, and O. K. Andersen, Phys. Rev. B **49**, 16223 (1994).
[38] M. Eibschütz, E. Hermon, and S. Shtrikman, J. Phys. Chem. Solids **28**, 1633 (1967).
[39] J. E. Jaffe and A. Zunger, Phys. Rev. B **29**, 1882 (1984).
[40] A. Marini, G. Onida, and R. Del Sole, Phys. Rev. Lett. **88**, 016403 (2001).
[41] X. Wu, D. Vanderbilt, and D. R. Hamann, Phys. Rev. B **72**, 035105 (2005).